Supplemental Material : Experimental Determination of Gamma-Ray Polarization from Strong-Field Nonlinear Compton Scattering

Content:

I Normalized NCS gamma-ray yield versus interaction distance.

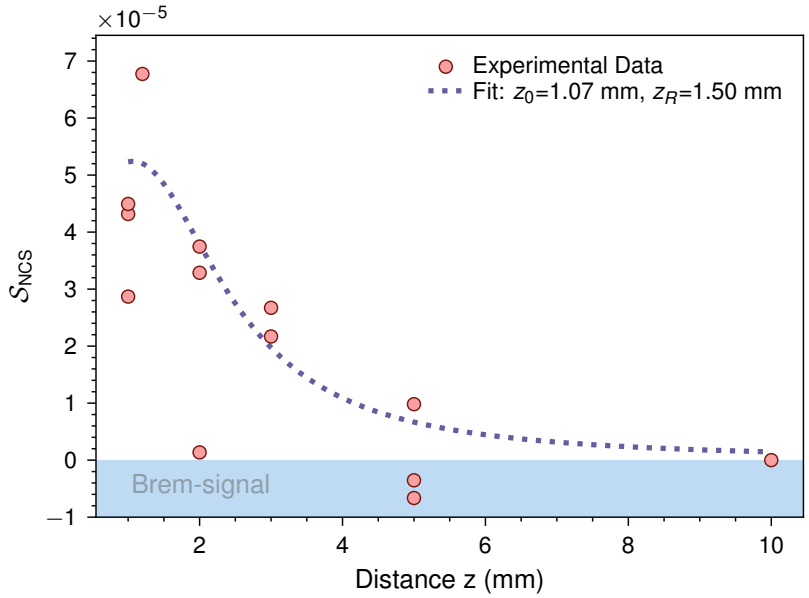

Fig. S1: **Normalized NCS gamma-ray yield versus interaction distance.** The normalized yield $\mathcal{S}_{\mathrm{NCS}} \equiv \Sigma_{\mathrm{NCS}}/(Q_e \cdot \langle \varepsilon_e^2 \rangle)$, defined as the background-subtracted NCS signal divided by the electron beam charge and the mean square electron energy, is plotted against the longitudinal displacement z of the PM. The displacement modulates the peak laser intensity a_0 at the collision point. The data are fitted (solid line) with function $\mathcal{S}_{\mathrm{NCS}}(z) = A\left[1 + (z - z_0)^2/z_R^2\right]^{-1}$. The obtained values for z_0 and z_R are given in the legend. The blue shading indicates the simulated bremsstrahlung background component, which is subtracted from the total signal at the largest displacement ($z = 10$ mm), where the residual NCS contribution is small but non-negligible. Its consistency with the combined model of bremsstrahlung plus NCS is examined in Fig. S2.

As shown in Fig. S1, the experimental data for $\mathcal{S}_{\mathrm{NCS}}$ are well-fitted by this function (solid line). The normalized yield is highest at the optimal overlap position and decreases monotonically as the mirror is retracted and a_0 diminishes. The fitted Rayleigh length $z_R \approx 1.50$ mm is larger than the ideal value calculated from the initial laser parameters (~ 0.48 mm). This is attributed to several experimental factors: (i) the convolution of the finite-sized electron beam with the laser intensity profile, which broadens the measured spatial response; (ii) wavefront distortion introduced by the plasma mirror ; and (iii) modification of the laser's spatiotemporal properties during the interaction. The latter includes nonlinear frequency upshifts and spectral broadening as the pulse propagates through the underdense plasma and reflects from the overdense plasma mirror, which alter the effective wavelength and beam caustic. Despite these complexities in precisely determining the absolute laser profile at the interaction point, the strong functional dependence of $\mathcal{S}_{\mathrm{NCS}}$ on PM displacement provides evidence for the laser-driven origin of the signal.

It is important to note that the data points in Fig. S1 represent the net NCS yield obtained after subtracting a shot-specific bremsstrahlung background simulated with GEANT4, using the measured electron energy spectrum as input. At the farthest position ($z = 10$ mm), where the laser intensity is reduced to $a_0 \sim 0.4$ (as shown by the dotted line), a small NCS signal remains. The validity of this background subtraction approach, and the consistency of the total (bremsstrahlung + NCS) model with the experimental detector response, is demonstrated in the following analysis (Fig. S2).

The derivation and extraction of the normalized yield $\mathcal{S}_{\mathrm{NCS}}$, as presented in Fig. S1, are detailed below.

1. **Theoretical scaling and definition.** The definition of $\mathcal{S}_{\mathrm{NCS}}$ is grounded in the theoretical scaling of nonlinear Compton scattering. In the nonlinear regime ($a_0 > 1$), the total energy radiated by a single electron, W_{rad}, can be evaluated as the product of the number of emitted photons and their average energy. This follows from the approximate number of emitted photons, $N_\gamma \approx 5\alpha\hbar\omega_0 a_0\tau/(\sqrt{3}m_e c^4)$ [1], and the average photon energy, $\overline{\omega}_\gamma \approx E_e\chi_e$, where the electron quantum parameter is $\chi_e = (2\hbar/(m_e^2c^4))\omega_0 E_e a_0$. Therefore, the total radiated energy by a single electron scales as $W_{\mathrm{rad}} \approx N_\gamma\overline{\omega}_\gamma \propto a_0^2E_e^2$.Consequently, extending this to an electron beam with total charge Q_e and mean square energy $\langle E_e^2\rangle$, the integrated NCS signal deposited in the calorimeter is expected to scale as $\Sigma_{\mathrm{NCS}} \propto a_0^2 Q_e\langle E_e^2\rangle$. To decouple the laser intensity dependence from electron beam fluctuations, we define the normalized yield as:

$$\mathcal{S}_{\mathrm{NCS}} \equiv \frac{\Sigma_{\mathrm{NCS}}}{Q_e \cdot \langle E_e^2\rangle}.$$

   By definition, $\mathcal{S}_{\mathrm{NCS}}$ serves as a direct proxy for the squared laser intensity, $\mathcal{S}_{\mathrm{NCS}} \propto a_0^2$.
2. **Bremsstrahlung background subtraction.** The total signal recorded in experiment, Σ_{tot}, comprises contributions from both NCS and bremsstrahlung. To isolate the NCS component Σ_{NCS}, a shot-specific bremsstrahlung background was modeled using GEANT4 simulations [2–4], with the experimentally measured electron energy spectrum $\mathrm{d}N_e/\mathrm{d}E$ as input. This simulation accounts for the full beamline geometry and detector response. For each interaction shot, the net NCS signal was then extracted as $\Sigma_{\mathrm{NCS}} = \Sigma_{\mathrm{tot}} - \Sigma_{\mathrm{brems}}$, where Σ_{brems} is the integrated simulated bremsstrahlung signal.
3. **Spatial profile fitting.** The longitudinal variation of the normalized yield $\mathcal{S}_{\mathrm{NCS}}(z)$ traces the on-axis evolution of the laser intensity $a_0^2(z)$. Assuming a Gaussian focal spot, the intensity follows a Lorentzian profile:

$$a_0^2(z) \propto \left[1 + \frac{(z - z_0)^2}{z_R^2}\right]^{-1},$$

   where z_0 is the focal position and z_R is the Rayleigh length. The experimental data were fitted with the corresponding zero-baseline Lorentzian function[5]:

$$\mathcal{S}_{\mathrm{NCS}}(z) = A\left[1 + \frac{(z - z_0)^2}{z_R^2}\right]^{-1}.$$

   The best-fit parameters (A, z_0, z_R) were extracted using a nonlinear least-squares algorithm and are provided in Fig. S1.

II Calibration of the LYSO-PX detector response.

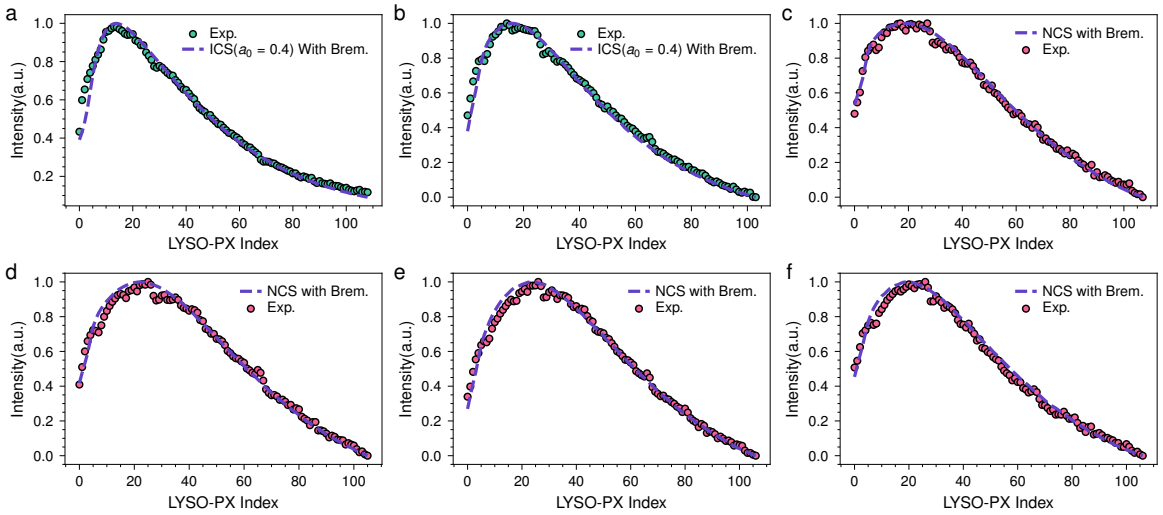

Fig. S2: **Spectral fitting of the LYSO-PX detector response at varying interaction distances. a, b**, Experimental energy deposition profiles (teal circles) for the PM positioned at 10 mm from the gas jet nozzle trailing edge. The data are fitted using a linear inverse Compton scattering (ICS) model with $a_0 = 0.4$ combined with the bremsstrahlung background. **c**, PM at 3 mm; **d**, PM at 2 mm; **e, f**, PM at 1 mm (the position selected for polarization measurements). For these three configurations, the data (pink circles) are fitted using a nonlinear Compton scattering (NCS) model combined with the bremsstrahlung background.

To validate the spectral decomposition framework and to map the transition from linear to nonlinear Compton scattering, we performed a systematic scan of the PM position, as shown in Supplementary Fig. S1. For each position, the bremsstrahlung background was modeled using GEANT4 with the measured electron spectrum as input, and the Compton scattering component was calculated using the LMA-based CAIN code. The total simulated signal was then compared with the experimental LYSO-PX energy deposition profiles.

Figures S2a and b show the results for the PM positioned at 10 mm from the gas jet nozzle trailing edge. At this large displacement, the laser is significantly defocused, yet not completely absent. The experimental data (teal circles) are well reproduced by a model combining the bremsstrahlung background and linear inverse Compton scattering (ICS) with $a_0 = 0.4$. This fitted value is consistent with the expected scaling from the spatial profile measurement (Supplementary Fig. S1), which shows that the integrated signal is proportional to a_0^2 and confirms that the residual laser intensity at 10 mm corresponds to $a_0 \approx 0.42$.

As the PM is moved closer to the nozzle, the laser intensity increases substantially, driving the interaction into the nonperturbative regime. Figures S2c–f present the results for PM positions of 3 mm, 2 mm, and 1 mm (the latter being the optimal position selected for polarization measurements). For these configurations, the experimental data (pink circles) are fitted using a nonlinear Compton scattering (NCS) model combined with the bremsstrahlung background. The fits accurately reproduce the measured energy deposition profiles across the full range of photon energies.

The robust agreement between the theoretical models and experimental data across all PM positions validates the spectral decomposition framework and captures the transition from linear to nonlinear Compton scattering. This systematic verification also provides confidence in the extracted a_0 values used in the polarization analysis.

III Determination of the effective laser intensity via spectral decomposition.

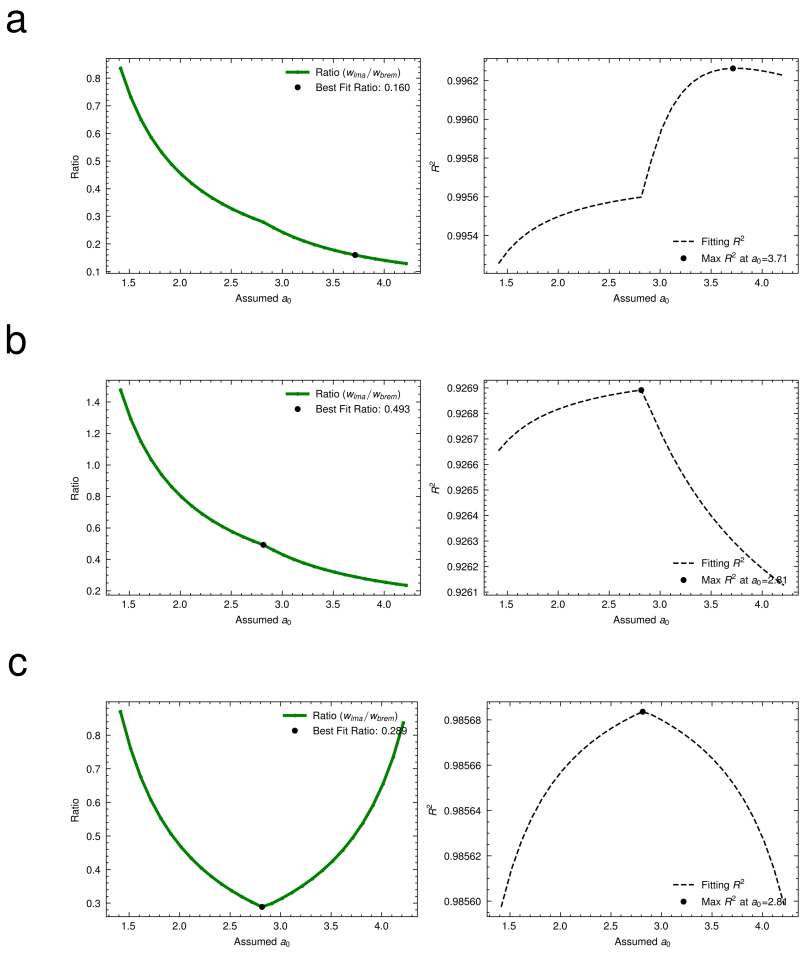

Fig. S3: **Determination of the effective laser intensity via spectral decomposition. a-c**, Parameter retrieval analysis for the three independent interaction events in Fig. 3 of the paper. For each assumed a_0, the experimental LYSO-PX energy deposition profile is fitted with a linear combination of the simulated bremsstrahlung background (w_{brem}) and the NCS response (w_{lma}). The left panels show the optimal signal ratio $w_{\mathrm{lma}}/w_{\mathrm{brem}}$ as a function of a_0 (green solid lines). The right panels display the corresponding goodness-of-fit R^2 (black dashed lines). The global maximum of the R^2 curve (black dots) identifies the effective laser intensity for each shot ($a_0 = 3.71$, 2.81, and 2.81, respectively).

To quantitatively extract the effective laser intensity a_0 at the collision point from the measured LYSO-PX calorimeter signals, we developed a spectral decomposition framework that is applied on a shot-by-shot basis. For each assumed a_0, we constructed a theoretical NCS spectrum using the Locally Monochromatic Approximation (LMA) as implemented in the CAIN code. The bremsstrahlung background was independently simulated using GEANT4 with the experimentally measured electron energy spectrum as input, accounting for the full detector geometry and response. The total modeled signal for a given a_0 was then formed as a linear combination of the NCS component and the

bremsstrahlung background. For each a_0, the optimal weight ratio $w_{\mathrm{lma}}/w_{\mathrm{brem}}$ was determined by minimizing the residual error between the model and the experimental data.

The analysis results for three representative high-signal shotsare presented Fig. S6a-c. The left panels show the best-fit signal ratio as a function of the assumed a_0 (green solid lines). The right panels display the corresponding goodness-of-fit, quantified by the coefficient of determination R^2 (black dashed lines). The R^2 value exhibits a clear global maximum at a specific a_0 for each shot, marked by black dots. These maxima identify the effective laser intensities as $a_0 = 3.71$, 2.81, and 2.81, respectively. The corresponding optimal signal ratios at these intensities are indicated by black dots in the left panels.

IV Evaluation of electron energy loss due to bremsstrahlung.

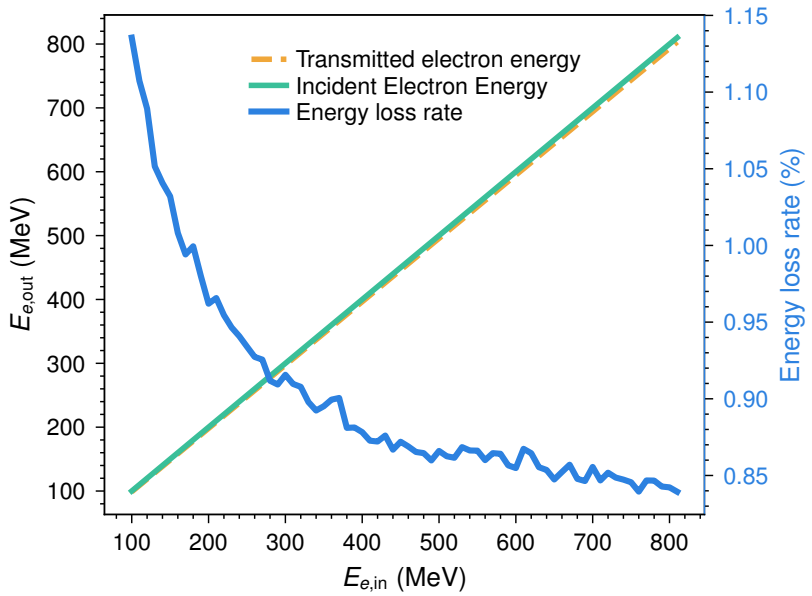

Fig. S4: **Evaluation of electron energy loss due to bremsstrahlung.** Comparison between the incident electron energy (green solid line) and the calculated average electron energy after propagating through the plasma mirror substrate (yellow dashed-dotted line), and the corresponding energy loss ratio (blue solid line, right axis). The simulation covers incident energies from 100 to 800 MeV. The energy loss ratio decreases from 1.14% at 100 MeV to 0.84% at 800 MeV, confirming that bremsstrahlung in the substrate induces negligible degradation of the electron beam.

The validity of using the post-interaction electron spectrum, measured by the downstream electron spectrometer, as the input for the full GEANT4 modeling (including bremsstrahlung and NCS detector response) rests on two key considerations: the negligible energy loss from nonlinear Compton scattering and the minimal energy loss from bremsstrahlung in the plasma mirror substrate.

First, the energy loss due to NCS can be estimated from the quantum parameter χ_e. For typical experimental parameters, electron energy $E_e = 600$ MeV, laser strength $a_0 = 3$, and laser wavelength $\lambda_0 = 800$ nm, the quantum parameter is $\chi_e = (2\hbar\omega_0/m_e^2c^4)E_e a_0 \approx 2.6\times10^{-3}$. In this regime ($\chi_e \ll 1$), the average fractional energy loss per photon emission is $\Delta E/E_e \sim \chi_e$. The total number of emitted photons per electron can be approximated as $N_\gamma \sim a_0\tau/T_0$, where $\tau = 28$ fs is the pulse duration. This yields $N_\gamma \sim 30$, and the total relative energy loss $\sim N_\gamma\chi_e \sim 8\times10^{-2}$, which is entirely negligible.

Second, the energy loss from bremsstrahlung as the electron beam traverses the plasma mirror substrate was evaluated via GEANT4 simulations. As shown in Fig. S6, the average electron energy after passing through the substrate deviates from the incident energy by less than 1.2% over the entire experimental energy range. More specifically, the energy loss ratio (blue solid curve) decreases from 1.14% at 100 MeV to 0.84% at 800 MeV, consistent with the expected energy scaling of radiative losses. This small deviation is comparable to the typical energy resolution of the electron spectrometer and has a negligible impact on the subsequent NCS spectral modeling.

Taken together, these results confirm that the electron beam parameters measured after the interaction can be reliably used as input for the GEANT4 simulations of the bremsstrahlung background and for the LMA-based NCS simulations.

V PIC numerical simulation of the laser-plasma interaction process.

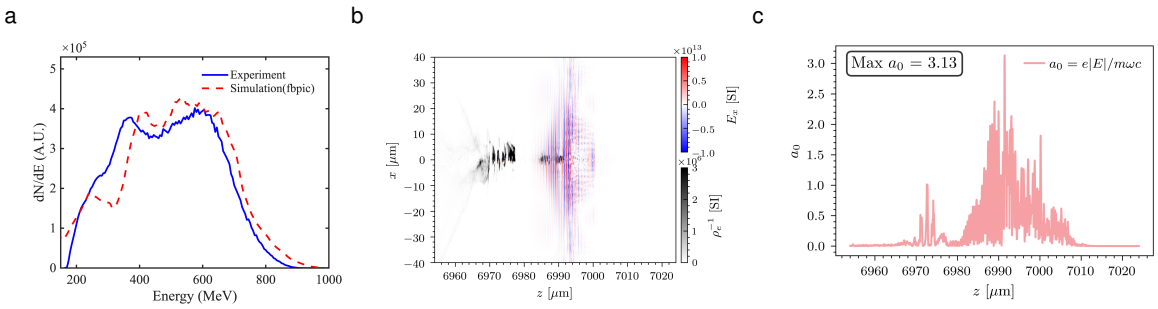

Fig. S5: **a,** Comparison between the experimentally measured electron energy spectrum (blue solid line) and the spectrum obtained from 3D FBPIC simulations (red dashed line). **b,** Snapshot of the simulated transverse electric field distribution (E_x) of the focused laser pulse near the interaction point.**c,** Longitudinal profile of the normalized laser vector potential $a_0 = e|E|/m\omega c$ along the propagation axis (z). The simulation indicates a peak intensity corresponding to $a_0 \approx 3.1$.

To independently verify the laser intensity $a_0 \approx 3$ extracted from the experimental data, we performed quasi-3D particle-in-cell (PIC) simulations of the full laser-plasma interaction using the open-source code FBPIC. The simulations include the propagation of the drive laser pulse through the gas target, the generation and acceleration of the electron beam, the reflection of the laser pulse from the plasma mirror, and the subsequent collision of the reflected laser with the electron beam at the interaction point. The input parameters in the simulation are consistent with the experimental conditions. Specifically, the plasma target is 6.5 mm long, consisting of 0.5 mm linear density up- and down-ramps and a plateau electron density of 2.448×10^{18} cm^{-3}. The driving Gaussian laser pulse ($\lambda_0 = 800$ nm, $\tau = 28$ fs) is focused 1.1 mm from the front edge with a spot size $w_0 = 10.9$ μm and an initial amplitude $a_0 = 6$. A pre-ionized plasma mirror is placed at 7.0 mm with a plateau thickness of 800 μm and a density of 2.66×10^{22} cm^{-3}. The moving simulation box measures 70 μm $\times$ 120 μm (longitudinal $\times$ transverse) with spatial resolution $\Delta z \approx \lambda_0/20$ and $\Delta r = \lambda_0/10$, using $N_m = 2$ azimuthal modes. It is important to note that the PIC simulations describe only the laser field evolution and electron acceleration; the spectral modeling of NCS is performed using a separate numerical method.

The PIC simulations yield a peak laser intensity of $a_0 \approx 3.1$ at the collision point after reflection from the plasma mirror. This result is in close agreement with the value $a_0 \approx 3$ obtained from the experimental data analysis based on NCS signal decomposition, considering the experimental uncertainties (e.g., shot-to-shot fluctuations in laser energy and pointing, as well as variations in plasma mirror performance) and the inherent approximations in the PIC modeling. The consistency between the independently simulated a_0 and the experimentally extracted value provides strong cross-validation, confirming the reliability of the experimental methodology and the theoretical framework employed.

VI Geant4 simulation of the Compton polarimeter response.

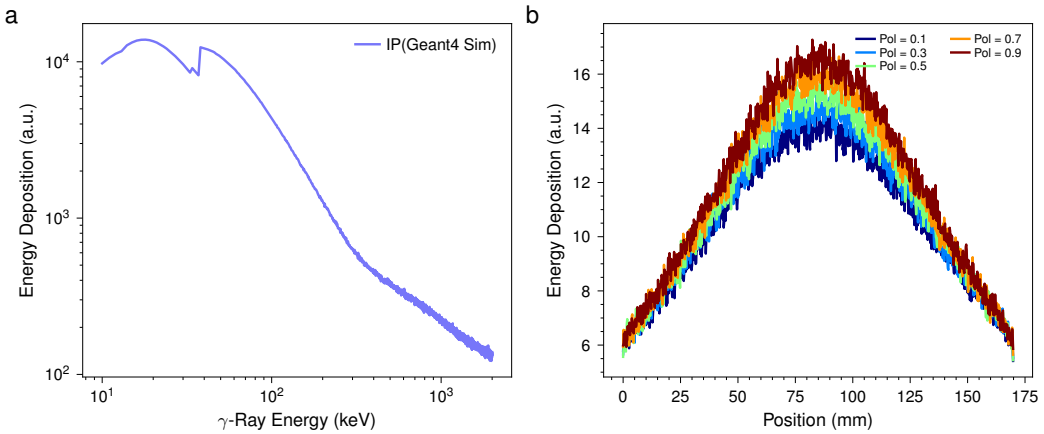

Fig. S6: **Geant4 simulation of the Compton polarimeter response. a**, Simulated energy deposition response of the Imaging Plate (IP) as a function of incident photon energy, obtained by modeling the full multilayer structure of the IP. **b**, Simulated azimuthal intensity profiles of Compton-scattered photons recorded on the top IP for incident gamma rays with varying degrees of linear polarization P (0.1 to 0.9).

To calibrate the Compton polarimeter and enable quantitative extraction of the gamma-ray polarization degree from the measured IP signal, we performed detailed GEANT4 simulations of the full detection system. The simulation model strictly implements the multi-layer physical structure of the Imaging Plate (IP), including the active phosphor layer, protective coating, and substrate, allowing accurate calculation of the energy deposition response as a function of incident photon energy. As shown in Fig. S6a, we tracked 10^6 incident photons per energy point to construct the energy-dependent deposition curve, which serves as the basis for converting the raw IP signal into deposited energy.

The azimuthal asymmetry measurement was simulated using the experimentally measured gamma-ray energy spectrum as the incident source. The gamma-ray beam impinged on a 2-cm-diameter graphite scattering target, consistent with the experimental geometry. Scattered photons were recorded on the top and side IPs, and the intensity profiles were obtained by integrating the deposited energy along the beam propagation direction (z). Fig. S6b shows the simulated azimuthal profiles for incident beams with varying degrees of linear polarization P ranging from 0.1 to 0.9. The spatial modulation of the profile-quantified by the slope of the intensity variation increases monotonically with P, demonstrating that the detector response is highly sensitive to the polarization state of the incident gamma rays. This simulated calibration library provides a robust reference for extracting the experimental polarization degree by comparing the shape of the measured IP profile with the simulated profiles, as described in the main text and shown in Fig. 4.

VII Raw photoneutron data and incident photon spectra.

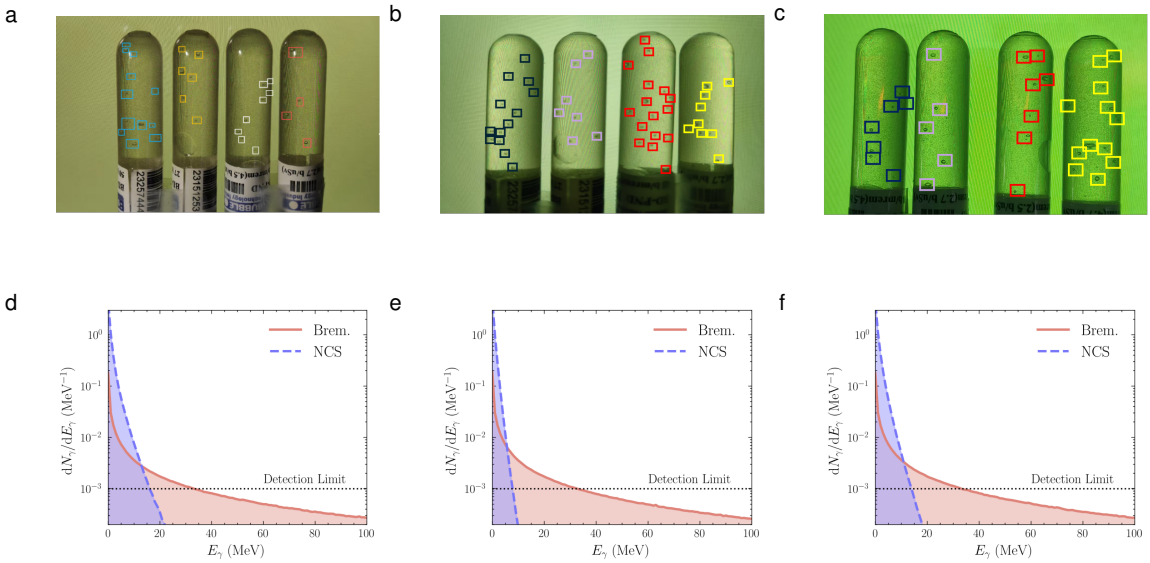

Fig. S7: **Raw photoneutron data and incident photon spectra. a-c,** Photographs of the bubble detectors used for polarimetry. The asymmetry in bubble counts between detectors at different azimuthal angles directly encodes the polarization information. **d-f** The deconvolved photon energy spectra incident on the D_2O target for three different shots. The spectra are decomposed into the polarized nonlinear Compton Scattering signal (NCS, blue dashed line) and the unpolarized Bremsstrahlung background (Brem., red solid line).

References

[1] Thomas, A. G. R., Ridgers, C. P., Bulanov, S. S., Griffin, B. J. & Mangles, S. P. D. Strong radiation-damping effects in a gamma-ray source generated by the interaction of a high-intensity laser with a wakefield-accelerated electron beam. *Phys. Rev. X* **2**, 041004 (2012). URL https://link.aps.org/doi/10.1103/PhysRevX.2.041004.

[2] Agostinelli, S. *et al.* Geant4—a simulation toolkit. *Nucl. Instrum. Methods Phys. Res. A* **506**, 250–303 (2003). URL https://www.sciencedirect.com/science/article/pii/S0168900203013688.

[3] Allison, J. *et al.* Geant4 developments and applications. *IEEE Trans. Nucl. Sci.* **53**, 270–278 (2006).

[4] Allison, J. *et al.* Recent developments in geant4. *Nucl. Instrum. Methods Phys. Res. A* **835**, 186–225 (2016). URL https://www.sciencedirect.com/science/article/pii/S0168900216306957.

[5] Salamin, Y. I. & Keitel, C. H. Electron acceleration by a tightly focused laser beam. *Phys. Rev. Lett.* **88**, 095005 (2002). URL https://link.aps.org/doi/10.1103/PhysRevLett.88.095005.